Analysis of a castable refractory using the wedge splitting test and cohesive zone model

R Vargas, J. Neggers, R B Canto, J A Rodrigues, François Hild

Analysis of a castable refractory using the wedge splitting test and cohesive zone model

R. Vargas[a,], J. Neggers[b], R. B. Canto[a], J. A. Rodrigues[a], F. Hild[b]

[a] *Federal University of Sao Carlos (UFSCar)*
Graduate Program in Materials Science and Engineering
Rodovia Washington Luis, km 235, 13565-905, São Carlos-SP, Brazil
[b] *Laboratoire de Mécanique et Technologie (LMT)*
ENS Paris-Saclay, CNRS, Université Paris-Saclay
61 avenue du Président Wilson, 94235 Cachan, France

Abstract

A cohesive zone approach is applied to the Wedge Splitting Test (WST) using the finite element code Abaqus to obtain the tensile strength, the fracture energy and insight about the crack wake region. A Finite Element Model Updating (FEMU) method, with a cost function based on the measured load (FEMU-F), is used to calibrate the sought parameters. Digital Image Correlation (DIC) provided the kinematic boundary conditions, and the images were also used to define the geometry for the finite element analysis. Besides the fracture energy analysis and the experimental load, gray level images and displacement fields are analyzed in order to validate the results. The cohesive region is active in the whole analyzed test as confirmed by estimates using the cohesive length.

Keywords: Cohesive zone model, digital image correlation, finite element model updating, wedge splitting test, castable refractory

1. Introduction

Refractory castables are ceramic materials with a fine matrix and coarser aggregates, which are utilized in transformation industries such as steel making and oil refineries [1, 2, 3]. Their main goal is to ensure functional properties

*Corresponding author
Email address: hild@lmt.ens-cachan.fr (F. Hild)

at high temperatures and corrosive environments, thereby calling for complex processing of various materials [3]. In these environments with considerable thermal shocks between processing cycles, it is not optimal to prevent crack initiation [4]. The applied approach consists in tailoring the microstructure with suitable compositions to make crack propagation difficult. The most important toughening mechanisms are extrinsic resulting from the interaction of the crack with the microstructure. Some examples [5, 6] are crack branching, microcrack formation to alleviate stresses at the crack tip, bridging and phase transformations (*e.g.,* tetragonal to monoclinic zirconia transformation).

To study these toughening mechanisms, stable crack propagation tests may be performed in laboratory conditions. The Wedge Splitting Test (WST) allows such fracture tests to be conducted, even on quasi-brittle materials, by decreasing the elastic energy stored in the testing machine thanks to a wedge and cylinders to apply an opening (mode I) load [7, 8]. This test is commonly used for obtaining the fracture energy of these materials, which is a key property for understanding the thermal shock resistance of refractories [9, 10]. The advantage of this test includes a high fracture surface area to specimen volume ratio, which is needed for obtaining representative results if big aggregates are used for toughening purposes [8].

The WST may be combined with Digital Image Correlation (DIC) for studying crack propagation. DIC is based on tracking material points during the loading of the sample [11, 12, 13]. It is a full-field measurement technique instead of providing local data points obtained by, say, conventional extensometry. Recently, several studies have reported on how to treat such results and obtain further information from WSTs [14, 15, 16, 17, 18, 19].

If toughening mechanisms are activated during fracture, it is hard to define a "binary" crack, with either a fully broken or fully intact material. A Fracture Process Zone (FPZ) is usually defined, where some damage has already occurred but some tractions between the crack surfaces remain [20, 21]. In that case, a Cohesive Zone Model (CZM) can be used [22]. The CZMs define the traction-separation law, which accounts for the fracture process. Several studies use

CZMs in Finite Element Analyses (FEA) for simulating fracture in quasi-brittle materials [21, 23, 24, 25, 26].

The calibration of cohesive zone properties with DIC measurements was addressed in various studies, mostly for modeling composites and/or adhesives. Measured displacements were used as Boundary Conditions (BCs) and inner nodal displacements in the objective function to identify the cohesive properties of fiber-reinforced metallic laminate. Discussions about how to obtain elastic and cohesive properties by minimizing the gap between measured and calculated displacements were also reported for a fiber-reinforced cementitious material [27], and for plastic and PMMA with adhesive [28]. Reference [29] presents a sensitivity analysis in order to analyze the most relevant region for identifying a CZM with full-field measurements. The sensitivity for the identification of cohesive parameters for an adhesive bonded structure is discussed in Ref. [30]. The authors concluded that higher sensitivity for the cohesive strength may be reached at pre-peak, and for the fracture energy with post-peak data. Traction-separation laws could be accessed directly with the kinematics of a Double Cantilever Beam test for composite materials [31]. The importance of using load data to identify a mixed-mode CZM for a composite was highlighted in another study [32]. Conversely, mixed-mode CZMs were calibrated without the need for force data, only using the images of the experiment on a microelectronic device [33].

Some studies also showed the feasibility of combining DIC and CZM for other materials. In Ref. [34], a multiscale setup is introduced for analyzing a photodegradable copolymer. Elastic and cohesive properties for concrete materials were identified with the Boundary Element Method coupled with DIC measurements [35]. Failure in metals was modeled with a CZM, which was calibrated with DIC data [36]. Micrometer-scale mechanisms in PMMA could be related to a traction-separation law using images taken close to the crack tip [37]. No study on castable refractories was found with such approaches.

In the present work, the parameters of a macroscale CZM for mode I fracture are calibrated with a single WST by coupling DIC measurements, load data and

FEAs performed with the commercial code Abaqus [38] for a castable refractory. First, the identification framework is introduced, then followed by the methods and definition of the parameters to be calibrated. Last, the results are shown and compared with previously reported data on different methodologies.

2. Calibration procedure

2.1. Experiment

The WST analyzed herein was performed on a class C, anti-erosive commercial refractory, with ultra low cement content. The detailed chemical composition and heat treatment of the material are reported in Ref. [15]. Its processing and microstructure may lead to an increasing R-curve behavior with weakly bonded grains and initiated microcracks due to anisotropic phases and differential thermal expansions. The sample size was 100 mm in length, 100 mm in height and 72.5 mm in thickness. The geometry is shown in Fig. 1 along with the mesh introduced in Section 2.3. It is possible to see the sample and the loading devices (*i.e.,* wedge, cylinders and blocks). Two grooves (i.e., vertical notches, evidenced in the right image in Figure 1) are machined on the two opposite faces of the sample to reduce the local thickness and guide the crack propagation vertically [19].

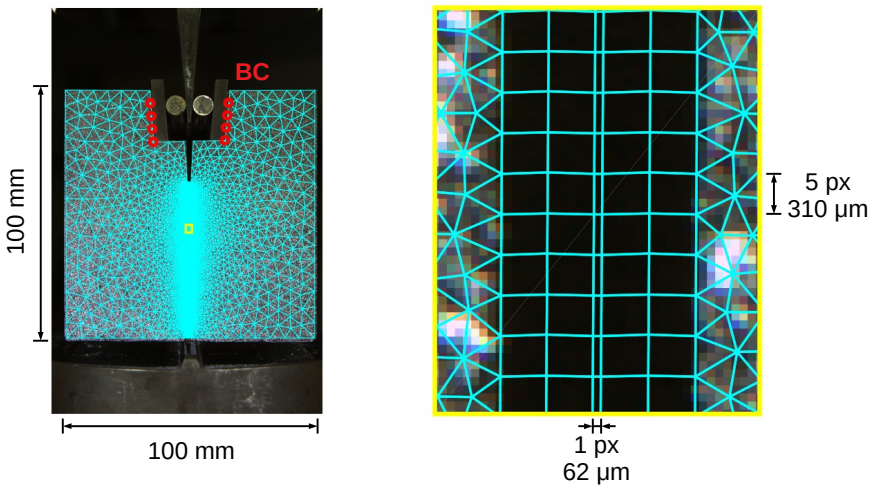

Figure 1: Sample geometry, with the FE mesh superimposed (left). The loading parts are visible at the top of the image. The red circles mark the nodes where the BCs are applied (see Section 2.3). The yellow box is zoomed (right), showing the mesh aligned with the groove edges. Triangular elements are used out of the groove, and Q4 quadrilaterals inside. The thin strip of elements in the middle of the groove shows the cohesive elements, which are collapsed to zero thickness for the present analyses.

The Young's modulus (E) and Poisson's ratio (ν) used for the investigated methods are equal to 17 GPa (measured by the bar resonance method [39]), and 0.2, respectively. The fracture energy calculated as the mean R-curve value (obtained by Integrated-DIC) is of the order of 68 J/m^2 [19]. The test was driven by setting the velocity of the machine actuator to 1.3 µm/s, and 313 pictures (reference + 312) were taken for both faces of the specimen at a rate of one picture each 8 s. The images were simultaneously acquired with two Canon T5 cameras with 28–135 mm lenses, with the illumination provided by LEDs. The 14-bit images captured at a definition of 2601×1733 pixels are up-sampled to 16-bit images with a dynamic range of approximately 60,000 gray levels. The imaged physical size of one pixel was 62 µm. A random speckle pattern was sprayed onto the specimen surfaces to increase the image contrast and improve the DIC resolution.

The horizontal force versus the splitting displacement, averaged from DIC measurements on opposite sides of the groove, is shown in Figure 2. The red circles mark the envelope of the curve that will be used by the identification routine with always increasing opening displacements. Let us note that since the test was interrupted before final failure of the sample, only a lower bound to the work of fracture, and to the fracture energy can be obtained [19].

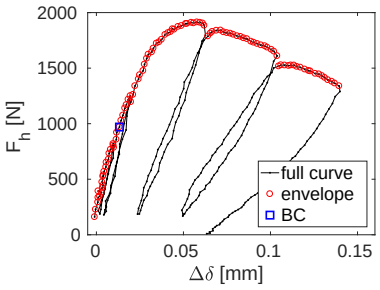

Figure 2: Horizontal force (*i.e.,* 5.715 times the vertical force) versus splitting displacement $\Delta\delta$ averaged on both sides of the sample. The images corresponding to the displacement envelope used in the identification are marked as red circles. Image no. 39 used for the BC_c parameter as explained in Section 2.6 is shown as a blue square.

Given the fact that the first picture was not acquired at zero load and a nonlinear model will be used, the displacement field accounting for this load offset is an additional unknown when calibrating constitutive parameters [40]. This is in particular true for cohesive zone models [32]. Image no. 39, highlighted with a blue square, is chosen for the BC corrections (see Section 2.6) since it is considered to be in the linear elastic regime (*i.e.,* 50% of the maximum force) and with higher displacement levels than the first images, thus being less affected by acquisition noise. Further details on the same experiment can be found in Refs. [15, 19].

2.2. Digital Image Correlation

In global DIC, the displacement field $\mathbf{u}_{DIC}$ is measured by considering that every pixel $\mathbf{x}$ within the Region Of Interest (ROI) in the reference image f is present in the deformed (*i.e.,* in a loaded state) image g but has moved by

$\mathbf{u}_{DIC}$ so that the displacement field globally minimizes the gap to gray level conservation

$$\phi^2 = \sum_{\text{ROI}} \left[f(\mathbf{x}) - g(\mathbf{x} + \mathbf{u}_{DIC}(\mathbf{x})) \right]^2, \tag{1}$$

which is the L2-norm of the gray level residuals $\rho(\mathbf{x})$. In order to ensure a good conditioning of this minimization and its robustness to noise, one more consideration is added to regularize the kinematics of a group of pixels, namely, it consists in expressing the sought displacement field as

$$\mathbf{u}_{DIC}(\mathbf{x}) = \sum_{i=1}^{N} \upsilon_i \mathbf{\Psi}_i(\mathbf{x}), \tag{2}$$

in which υ_i are the degrees of freedom, and $\mathbf{\Psi}$ selected vector fields. In such a framework, the measured displacements are obtained as

$$\{\boldsymbol{\upsilon}_{\text{DIC}}\} = \arg\min_{\{\boldsymbol{\upsilon}\}} \phi^2(\{\boldsymbol{\upsilon}\}), \tag{3}$$

where $\{\upsilon_{\text{DIC}}\}$ is the column vector gathering all amplitudes υ_i. A robust solution that works in most cases is choosing $\mathbf{\Psi}_i$ as finite element shape functions [41]. In this paper, the DIC procedure is performed with 3-noded linear elements in a finite element discretization [42] and will be referred to as T3DIC.

In the method presented herein, the first step is to run T3DIC since it will provide the necessary Boundary Conditions (BC) as explained in Section 2.3, and also displacement fields that can be compared with FE results. The mesh used for T3DIC and one displacement field (for image no. 263, *i.e.,* the last of the envelope, see Figure 2) is shown in Figure 3. The average element length is 37 pixels. This relatively large element size is chosen in order to reduce uncertainties due to acquisition noise. Care was taken to properly get the contour of the sample for avoiding identification artifacts and fully exploiting the image contrast as shown in the zoomed yellow rectangle. The central grooves are designed to guide the crack propagation along the center plane. However, castable refractories are prone to crack branching. For this experiment, it was shown that no major side branches were formed and only a single macrocrack had propagated in the groove [19].

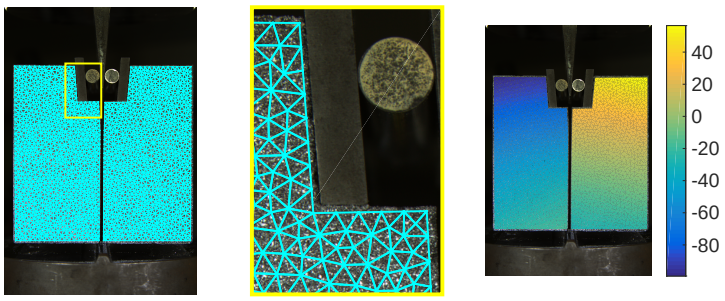

Figure 3: Sample geometry with superimposed T3DIC mesh (left). A zoom of the yellow rectangle is presented in the middle to show the contour of the mesh close to the loading plate. Horizontal displacement field expressed in μm for the last analyze image.

2.3. Numerical model

The FEA is performed with the commercial code Abaqus [38]. The geometry is taken from the image for ensuring that the measurement by T3DIC is performed exactly on the same region. The mesh is generated with GMSH [43] and shown in Figure 1, in which the nodes where the Dirichlet BCs are prescribed are shown with red circles. The corner node is not considered due to higher measurement uncertainty [44]. Since the exact same contours are used for the DIC and FE meshes in this region, a linear interpolation is performed to get the BCs. The groove (see Figure 1) has a reduced out-of-plane thickness. The yellow box corresponds to a zoom in the groove to show the mesh details. In the middle of the groove, a single strip of zero thickness cohesive elements (200 in the height) is added. Each face of the sample will be analyzed independently as a 2D model under plane strain hypothesis.

2.4. Identification strategy

The chosen identification scheme is based upon the Finite Element Model Updating (FEMU [45]) method. It is chosen to update the material parameters by reducing the difference between the calculated reaction force F_c and the experimentally measured force F_m. It is worth noting that the unload/reload

cycles are excluded from the identification since more complex CZMs would be necessary to accurately describe them [46]. Consequently, only the envelope of the curve is kept (*i.e.,* 100 out of the 312 images for which the crack is propagating, see Figure 2). It is chosen to have a continuous displacement of the actuator.

The identification methodology (*i.e.,* Newton-Raphson scheme) consists in a nonlinear least squares minimization of χ^2_F

$$\chi^2_F(\{\mathbf{p}\}) = \frac{1}{n_t \sigma_F^2} \sum_t \left(F_m(t) - F_c(t, \{\mathbf{p}\})\right)^2, \tag{4}$$

in which σ_F is the standard load uncertainty (on F_m), n_t the number of time steps, and F_c is the computed resultant of the reaction forces, which depends on unknown material parameters gathered in the column vector $\{\mathbf{p}\}$. If the only difference between the measured load levels $F_m(t)$ and $F_c(t, \{\mathbf{p}\})$ is acquisition noise, then χ_F will approach unity. Conversely, if there is a model error, then $\chi_F > 1$. By considering a given starting set of parameters $\{\mathbf{p}_n\}$ at iteration n, the minimization is performed by evaluating the correction $\{\delta\mathbf{p}\}$ on the linearized F_c

$$F_c(t, \{\mathbf{p}_n\} + \{\delta\mathbf{p}\}) \approx F_c(t, \{\mathbf{p}_n\}) + \frac{\partial F_c}{\partial \{\mathbf{p}\}}(t, \{\mathbf{p}_n\})\{\delta\mathbf{p}\}, \tag{5}$$

about the current estimate $\{\mathbf{p}_n\}$ of the sought parameters. The minimized quantity then becomes

$$\frac{1}{n_t \sigma_F^2} \sum_t \left(F_m(t) - F_c(t, \{\mathbf{p}_n\}) - \frac{\partial F_c}{\partial \{\mathbf{p}\}}(t, \{\mathbf{p}_n\})\{\delta\mathbf{p}\}\right)^2. \tag{6}$$

In Equation (6), the quantity to be minimized is quadratic in terms of $\{\delta\mathbf{p}\}$. Its minimization with respect to $\{\delta\mathbf{p}\}$ then leads to a linear system

$$[\mathbf{H}] \cdot \{\delta\mathbf{p}\} = \{\mathbf{h}\} \tag{7}$$

where $[\mathbf{H}]$ is the Hessian

$$[\mathbf{H}] = \sum_t \left(\frac{\partial F_c}{\partial \{\mathbf{p}\}}(t, \{\mathbf{p}_n\})\right)^\top \frac{\partial F_c}{\partial \{\mathbf{p}\}}(t, \{\mathbf{p}_n\}) \tag{8}$$

and $\{\mathbf{h}\}$ the right hand member

$$\{\mathbf{h}\} = \sum_t \left(F_m(t) - F_c(t, \{\mathbf{p}_n\})\right) \frac{\partial F_c}{\partial \{\mathbf{p}\}}(t, \{\mathbf{p}_n\}). \tag{9}$$

Convergence is deemed successful when the root mean square (RMS) of the relative variation of the parameters is less than 10^{-2} between two subsequent iterations. The sensitivity fields $\frac{\partial F_c}{\partial \{\mathbf{p}\}}$ are computed via finite differences in which the perturbation with respect to each parameter is set to 1%. The framework of the identification methodology may be further discussed by the sensitivity analysis presented in Section 3.1 using the Hessian $[\mathbf{H}]$.

2.5. Cohesive law

In this work, the selected cohesive law is the so-called PPR (Park, Paulino and Roesler) model [47, 48]. It was considered since the built-in cohesive models may give unrealistic responses for mixed mode propagations [49]. It is implemented in Abaqus with a User ELement (UEL) subroutine[1] [48]. Apart from the groove where the crack propagates and the cohesive model is implemented, the remaining part of the specimen has a linear elastic behavior. The information about mode II propagation or compressive damage was not considered, but care was taken in the implementation so that it did not interfere with the reported results. Figure 4 shows the two parameters to be calibrated for the cohesive zone model used herein, namely, the cohesive strength σ_{max}, and the fracture energy J_c.

[1] https://paulino.ce.gatech.edu/PPR_tutorial.html

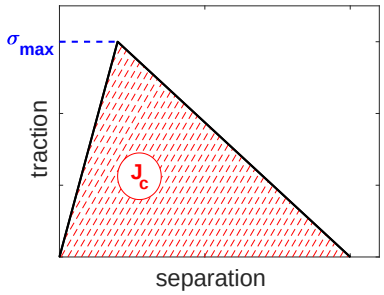

Figure 4: Schematic traction separation law highlighting the main parameters ($\sigma_{\max}$ and J_c) to be calibrated.

For the PPR model, the constitutive behavior for mode I includes the cohesive strength σ_{max}, and the fracture energy J_c. Two additional parameters are considered, namely, the initial slope λ_n and the shape parameter α. These last two parameters are chosen to be constant in the identification scheme. λ_n is kept equal to 0.005 for both cases [48], and considered as a small value within the stability limits [47]. The sensitivity to λ_n was tested and did not significantly affect the results. The parameter α however does change the softening response of the cohesive law. For the first case, its value is taken as 2 in order to approach a bilinear law [47] as shown in Figure 4. The second analyzed case considers $\alpha = 7$ to change the shape of the curve (Figure 11) to check if it better describes the considered test. Two built-in CZMs, namely, a bi-linear traction-separation law and the so-called Concrete Damaged Plasticity model, were also tested with parameters to replicate the studied case with $\alpha = 2$ and yielded very similar results [46]. For the sake of brevity, they are not discussed herein.

2.6. Boundary condition correction

One additional parameter is related to the non-zero load associated with the acquisition of the first image (Figure 2). It calls for a BC correction [32, 40] and will be designated as BC_c. In the experiment, the reference image was taken with a pre-load in order to remove any slack in the loading configuration.

Thus, the reference image of the unloaded state is unknown, and all measured displacements are performed with respect to the pre-load configuration.

The parameter BC_c introduced herein thus has to correct the kinematics from the unloaded state to the pre-loaded state. It is chosen to define BC_c as a multiplicative scalar of the displacement field related to a specific time step in the elastic regime of the experiment, and add it to the displacement fields for all time steps. The logical choice would be to consider the displacements of the very first images but they are small and consequently more affected by acquisition noise. Image 39 (*i.e.,* the 24th of the envelope, see Figure 2), which corresponds to approximately half of the maximum load, is chosen as a compromise of remaining in the linear part of the load but not too close to the noisier beginning. The corrected displacement fields $\mathbf{u}_{BC_c}$ read

$$\mathbf{u}_{BC_c} = (BC_c - 1) \cdot \mathbf{u}_{39}, \tag{10}$$

When BC_c is equal to 1, no correction is performed. It is expected that $BC_c > 1$ for the correction of the reference state with an opening displacement field, *i.e.,* a fraction of the displacement field measured in image 39. In the case of $BC_c < 1$, a contraction displacement field would be considered in the correction.

2.6.1. Initial parameters

The properties used for initializing the identification scheme are listed in Table 1. The cohesive strength σ_{max} was selected as the maximum T-stress measured in Ref. [19] with the method that provided more trustworthy results for the T-stress (*i.e.,* FEMU). The initial fracture energy J_c corresponds to its estimate based upon Integrated-DIC results [19]. The last parameter, BC_c, has its initial value set to one (*i.e.,* no BC correction would be needed).

Table 1: Initial parameters for the identification scheme.

σ_{max} [MPa]	J_c [J/m^2]	BC_c [-]
2	68	1

3. Results

3.1. Sensitivity analysis

Before performing the calibration of material parameters, a sensitivity analysis is performed [50]. Only the case $\alpha = 2$ is reported since the sensitivities are very close to those when $\alpha = 7$. The load sensitivities are defined as

$$S_F(t, \{\mathbf{p}_0\}) = \frac{\partial F_c}{\partial \{\mathbf{p}\}}(t, \{\mathbf{p}_0\}), \tag{11}$$

and approximated using a forward difference approach with a perturbation factor $\epsilon = 10^{-2}$ of each parameter. Figure 5 shows the computed load sensitivity S_F, indicating the influence of each parameter as a function of time. The influence of the parameter BC_c is very important at the beginning of the test. The peak influence of the cohesive strength σ_{max} occurs in the middle of the sequence of images, which is related to the part of the test where the measured force is high. The fracture energy J_c has higher sensitivity at the end of the test, which is to be expected since the crack has propagated a significant distance [15, 19]. For all parameters, the load sensitivities are significant (in comparison with the load uncertainty) for a one percent variation of each parameter. This result indicates that the parameters are expected to be identifiable with the considered test and identification procedure.

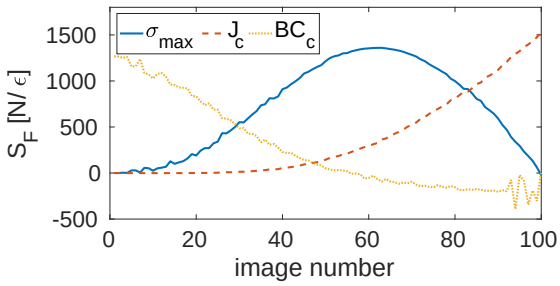

Figure 5: Force sensitivity to the parameters of the $\alpha = 2$ case. The blue solid line is the sensitivity to the cohesive strength σ_{max}, with a maximum sensitivity close to the middle of the test, *i.e.,* near the maximum splitting load. The red dashed line is related to the fracture energy J_c with a maximum sensitivity to the end of the test, after many elements are already damaged. The yellow dotted line corresponds to the BC correction BC_c, with maximum sensitivity at the beginning of the test where the displacements are very small.

Figure 6(a) shows the decimal logarithm of the values of the 3×3 Hessian ([**H**], see Equation (8)). The diagonal terms indicate the sensitivity to each property considered independently, and the off-diagonal members the cross influences between parameters. In the case of fully independent parameters, only the diagonal terms would be different from zero. As expected from the previous analysis, all parameters have very high sensitivities, and the conditioning of the system is very good (*i.e.,* less than 10). From this sensitivity analysis, it is confirmed that all parameters can be calibrated with the selected test and identification procedure.

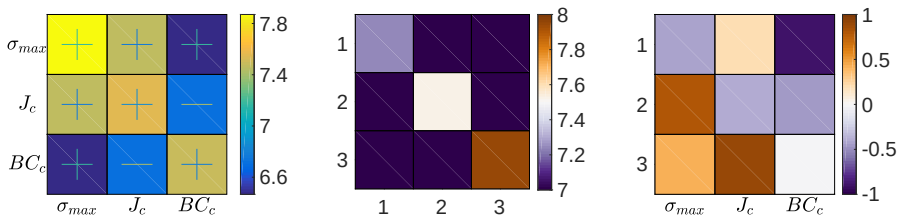

(a) (b) (c)

Figure 6: (a) Hessian of the identification procedure for the $\alpha = 2$ case shown as decimal logarithm. The diagonal terms show the sensitivity of each independent parameter. The off-diagonal terms show the cross influence between the parameters. (b) Decimal logarithm of the diagonalized Hessian. (c) Eigen column vectors associated with the diagonalization of the Hessian.

The decimal logarithm of the diagonalized Hessian is shown in Figure 6(b). Given the fact that the minimum eigen value of the Hessian is very high, there was no need for regularizing the Newton-Raphson scheme to ensure the definiteness of [**H**]. The first eigen value is dominant in BC_c and is almost independent of the other parameters. The second and the third eigen values are dominant in $\sigma_{\max}$ and J_c, in the same order of magnitude, showing that they are more correlated. Such conclusion is drawn from the eigen vectors reported in Figure 6(c).

3.2. Calibration results

Figure 7 shows the experimental and computed resultant forces for the two analyzed cases, *i.e.,* with the PPR model and for $\alpha = 2$ and $\alpha = 7$. The identified parameters give a very good fit of the experimental curve, which is a first validation of the model. The differences between both cases are very small.

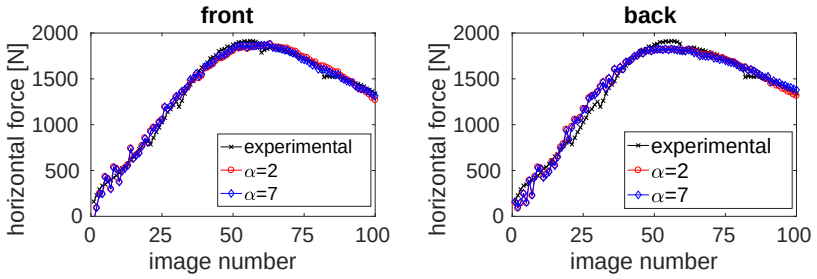

(a) (b)

Figure 7: Experimental and computed reaction forces on the converged state for the two analyzed cases, for the front (a) and back (b) faces of the experiment.

For easier comparison, the difference between the calculated and experimental forces, which have been normalized by the standard load uncertainty[2], are shown in Figure 8. Although some oscillations are seen, the mean value is plotted in dashed lines, showing that on average the error was of the order of twice the acquisition noise. This level is sufficiently small [32] to validate both cases. For the front face, $\alpha = 7$ provided slightly better results (RMS error of 1.5 as opposed to 1.8 when $\alpha = 2$), and for the back face $\alpha = 2$ was a bit better (RMS error of 2.0 against 2.1). Overall, considering only the force residuals, it is concluded that $\alpha = 7$ is (a bit) more suitable for the test studied herein. However, a bilinear model should not be excluded since its performance is also very good.

[2]The load uncertainty is equal to 0.1 % of the 5 kN load cell capacity, *i.e.,* 5 N for the vertical force, namely, of the order of 30 N for the horizontal force.

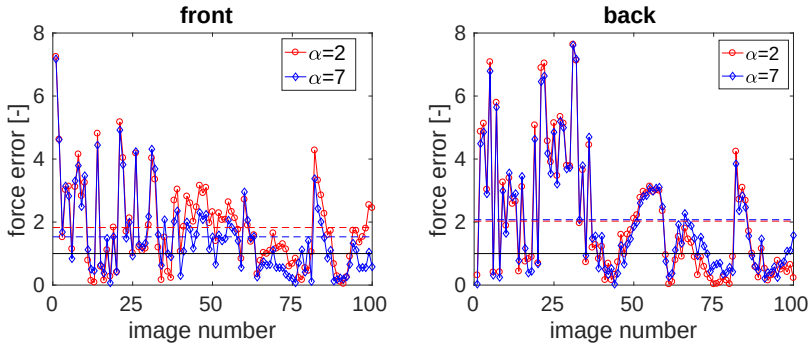

(a) (b)

Figure 8: Absolute reaction force residuals for the two cases normalized by the standard load uncertainty (solid lines), for both faces of the sample. The temporal average is shown as dashed lines.

The displacement fields were not used in the identification routine except at very few points as BCs in the FEA. The measured and computed displacement fields can thus be compared at any other location provided the computed displacement field corresponding to the reference image cancels out. For the calibrated parameters, the relative displacements (with respect to the pre-load configuration) are computed and then compared to the T3DIC kinematics at each time step of the test. These corrected FE results (whose mesh is shown in Figure 1) are interpolated onto the T3DIC mesh (Figure 3) and the RMS difference normalized by the standard displacement uncertainty is shown in Figure 9. The differences between front and back faces are mostly related to experimental inaccuracies, which are higher for the back face. The increasing trend shows that the numerical assumptions (*i.e.,* the constitutive law) are less true as the test goes on. However, the average error is of the order of 2.5 times the displacement uncertainty for the front face, and about 1.5 times for the back face. This level is sufficiently low [32] to give confidence in the model considered herein. The differences of the mean value between both cases is negligible (*i.e.,* of the order of 10^{-3}).

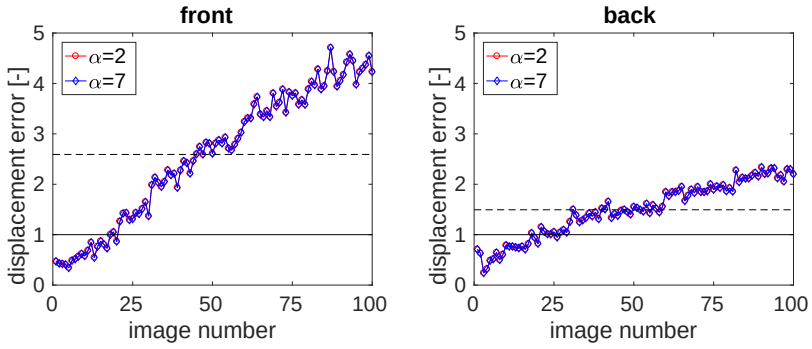

(a) (b)

Figure 9: RMS residual between computed and experimental displacements normalized by the T3DIC displacement uncertainty (solid lines). The temporal average is shown as dashed lines.

With the proposed framework, the gray level residuals from the FE results can also be checked. This is possible because measured displacements were prescribed as BCs in the numerical model, and the computed displacement fields were corrected to account for the fact that the reference configuration corresponds to the pre-loaded sample. The gray level residuals read

$$\rho_{FEA}(\mathbf{x},t) = f(\mathbf{x}) - g_t(\mathbf{x} + \mathbf{u}_{FEA}(\mathbf{x},t)) \tag{12}$$

where $\mathbf{u}_{FEA}$ is the computed displacement field, after taking out the pre-load kinematics related to BC_c, interpolated onto the T3DIC mesh. The same framework used for performing T3DIC may then be used to evaluate the gray level residuals. The RMS level of $\rho_{FEA}(\mathbf{x},t)$ performed over all pixel location $\mathbf{x}$ of the ROI normalized by the corresponding T3DIC residual $\rho_{DIC}(\mathbf{x},t)$

$$\frac{\mathrm{rms}_{\mathrm{ROI}}[\rho_{FEA}(\mathbf{x},t)]}{\mathrm{rms}_{\mathrm{ROI}}[\rho_{DIC}(\mathbf{x},t)]} \tag{13}$$

for each image is shown in Figure 10, where

$$\rho_{DIC}(\mathbf{x},t) = f(\mathbf{x}) - g_t(\mathbf{x} + \mathbf{u}_{DIC}(\mathbf{x},t)) \tag{14}$$

The former is only 50 to 60 % higher than the latter in which no hypothesis was made on the constitutive behavior. This observation further validates the

overall trends of both cases. As reported for the displacement residual, the mean value of the normalized gray level residual between both cases is of the order of 10^{-3}.

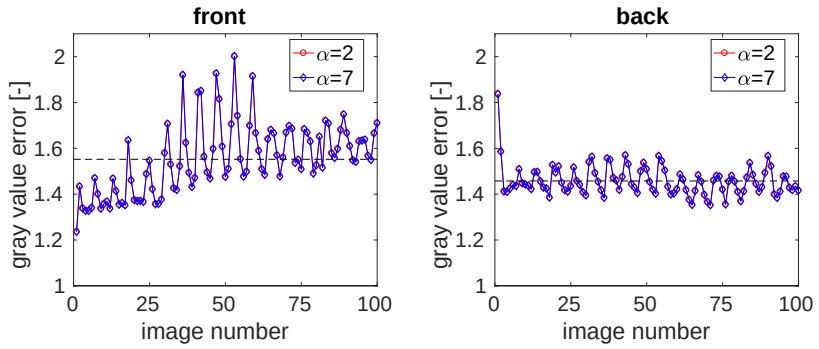

(a) (b)

Figure 10: Gray level residuals using FEA kinematics (ρ_{FEA}) normalized by the gray level residuals obtained from T3DIC (ρ). The temporal average is shown as dashed lines.

Figure 11 shows the traction vs. separation responses for each calibrated model. The curves represent the response of the most damaged element, *i.e.,* the closest element to the pre-crack, showing that no element was fully damaged (*i.e.,* the maximum level is equal to ≈ 0.85 and 0.75 when $\alpha = 2$ and $\alpha = 7$, respectively). It is worth remembering that complete propagation was not achieved since the experiment was performed until 70 % of the peak load (Figure 2).

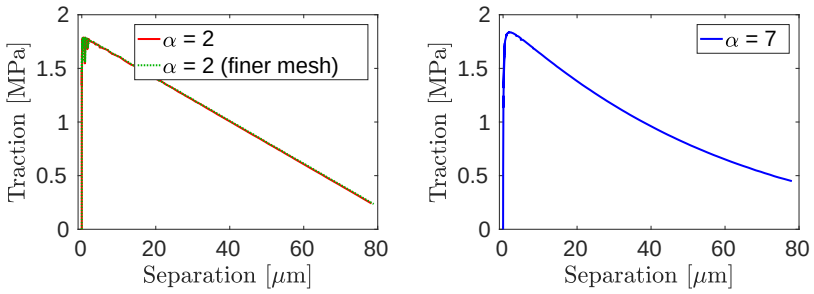

(a) (b)

Figure 11: Traction vs. separation responses of the most damaged element for the two cases calibrated with the front face data. The response for the mesh sensitivity analysis (discussed at the end of this section) is shown when $\alpha = 2$, where the main difference at the end of the curve is of the order of 0.01 MPa.

Table 2 gathers the calibrated parameters for each studied case when initialized with the set given in Table 1. The traction vs. separation curves (Figure 11) are similar for both cases, close to a bilinear response when $\alpha = 2$, and with a nonlinear softening when $\alpha = 7$. They all converged after at most five iterations of the FEMU-F procedure. It is possible to see that σ_{max} varies in the range 1.70 ± 0.15 MPa for the two cases; J_c has a difference of almost 20 % from $\alpha = 2$ to $\alpha = 7$, with a smaller difference if the same case is considered and both faces are compared. The BC_c difference highlights that the wedge was not fully aligned. It is possible to conclude that the wedge was applying more force on the back face of the specimen at the beginning of the test. It is worth noting that the cohesive strengths σ_{max} are of the same order of magnitude as the maximum T-stresses reported in Ref. [19].

Table 2: Converged parameters on the identification scheme for the two studied cases.

face	α	σ_{max} [MPa]	J_c [J/m^2]	BC_c [-]
front	2	1.79	82	1.314
	7	1.84	100	1.320
back	2	1.58	89	0.897
	7	1.59	115	0.906

Although the mesh is finer than classical guidelines for cohesive elements [51, 52, 53, 54] (*i.e.,* 200 elements in the total length of the propagation path, which will be shown to be less than the process zone length in Section 3.3.2), a mesh sensitivity analysis was performed with a finer mesh having more than 3 times the number of cohesive elements (*i.e.,* 620). When the subsequent FEMU-F procedure was initialized with the parameters calibrated with the coarser mesh, only one iteration was needed to reach convergence (*i.e.,* the parameter differences were less than 0.5 %). This observation proves that the two solutions are very close, which is confirmed in Figure 11(a) in terms of the traction separation law. From this analysis it is concluded that mesh convergence was achieved with the 200-cohesive element mesh. All the results of the next section were also checked for the two mesh densities and no tangible differences were observed. For the sake of brevity, they will not be presented.

3.3. Discussion

3.3.1. Fracture energy

In order to better understand the simulated fracture behavior, one last analysis is proposed. The displacements of the nodes of each cohesive element on the identification analysis are applied as BCs in a zip-like model, namely, only using the cohesive elements. With this approach, it is ensured that the same experimental kinematics is applied. It follows that the reaction forces at each node can be extracted. From the reaction forces, the tractions in each element and each time step are available. Using the traction / separation of each element, the dissipated energy can be computed. The vertical (mode II) displacements

and corresponding reaction forces are insignificant and are thus not accounted for hereafter.

The mode I tractions T_I are shown in Figure 12 for the front face. The image number on the x-axis is related to the time step for the envelope images (Figure 2). The y-axis is the vertical position of each node along the groove, *i.e.*, $y = 0$ is the node closest to the pre-crack and $y = 60$ mm the one at the bottom of the sample. A compressive zone develops after image no. 40, which hinders the propagation but does not stop the crack. Even though the color bar is fixed from -2 to 2 MPa for easier visualization, the minimum level is approximately -9 MPa. Similar figures are generated for the back face, which are reported in Appendix A (Figure 17).

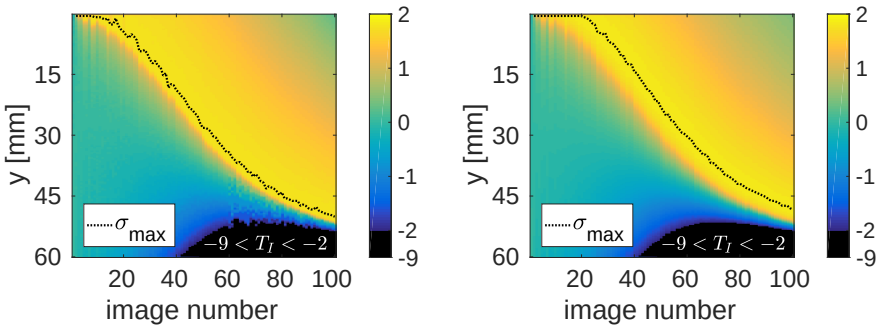

Figure 12: Normal traction (expressed in MPa) history for the front face when $\alpha = 2$ (a) and $\alpha = 7$ (b). The black dotted line shows the location for which the cohesive strength $\sigma_{\max}$ was reached.

It is worth noting that σ_{max} was not reached for the last elements since the test was not performed until final failure. For the same reason, non-vanishing tractions are still observed in the first elements. The region where the energy is being dissipated is large (*i.e.*, many damaged cohesive elements), with remaining cohesion even close to the pre-crack. Only the elements closest to the initial notch experience small traction levels, which indicates that their damage level is high. To determine the fractured surface, it is possible to consider an equivalent

damage variable for any CZM. For each node, the damage parameter is defined as

$$D = 1 - \frac{\sigma_I}{\sigma_{max}} \quad \text{when} \quad 0 < [\![u_I]\!] < \delta_c \tag{15}$$

where σ_I is the mode I traction (whose spacetime history is shown in Figures 12 and 17), $[\![u_I]\!]$ the mode I opening displacement, δ_c the maximum separation, and σ_{max} the cohesive strength. The damage variable history calculated with Equation (15) for the front face and both analyzed α is shown in Figure 13. Although the material is quasi-brittle, Figure 13 shows that the damage grows slowly. About two thirds of the sample have been damaged at the end of the reported test. Some cohesion remains along the whole propagation path (as already discussed above). However, there is a ligament in which no damage at all has occurred. The same trends are observed for the back face, as reported in Appendix A (Figure 18).

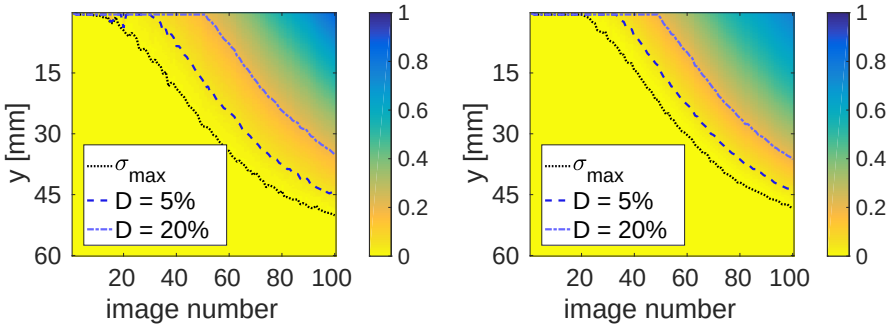

Figure 13: Damage history for the front face when $\alpha = 2$ (a) and $\alpha = 7$ (b). The black dotted line shows the location for which the damage variables starts to grow (*i.e.*, when the cohesive strength $\sigma_{\max}$ was reached).

The elementary fracture energy corresponds to the area under the cohesive response. It is obtained by integrating the opening displacement vs. traction responses of each cohesive element. At a given step, the dissipated energy is calculated by removing the elastic energy from the total work of each element. Figure 14 shows the dissipated energy for each cohesive element of the front face

of the analyzed cases. The maximum possible dissipated energy is equal to J_c (*i.e.,* 82 J/m^2 for $\alpha = 2$ and 100 J/m^2 for $\alpha = 7$). Not a single element reached this value, since the maximum level is found equal to 71 J/m^2 and 64 J/m^2, respectively. The same tendencies are observed for the back face (Figure 19).

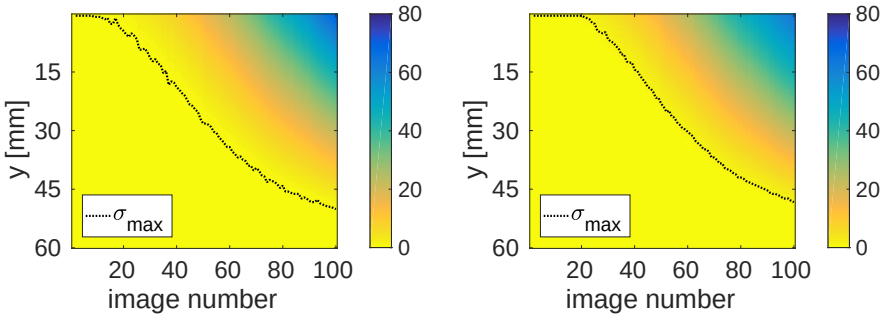

(a) (b)

Figure 14: Elementary dissipated energy (expressed in J/m^2) for the front face, with $\alpha = 2$ (a) and $\alpha = 7$ (b). The black dotted line shows the location for which the cohesive strength $\sigma_{\max}$ was reached.

Let us consider the cracked surface as the damaged area, *i.e.,* the region from the first to the last cohesive elements that reached σ_{max}. The total dissipated energy is calculated by multiplying the elementary dissipated energy (see Figure 14) by the element area, and summing the contributions of every element at each time step. The total dissipated energy is shown as a function of the "crack" length (as defined above) in Figure 15. An exponential interpolation describes the observed trends, which means that as the damaged zone grows, a bigger energy increment is needed to further propagation. Overall, the crack propagated a little farther and dissipated more energy in the back face, as seen in Figure 15. This result was expected from the conclusions analyzing the BC_c parameter (*i.e.,* tilted wedge applying more force on the back side). When $\alpha = 2$ case, the crack propagated a little farther and more energy was dissipated on both faces of the sample.

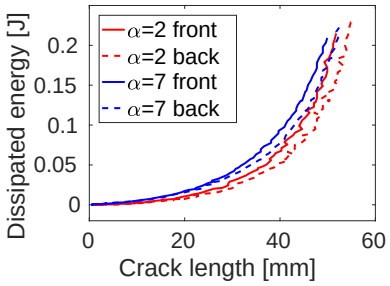

Figure 15: Dissipated energy in the analyzed test for the studied parameters. Solid lines represents the front face results, and the back face ones are in dashed lines.

To evaluate the global fracture energy, $\mathcal{G}_c$, let us consider E_{diss} as the total dissipated energy in the specimen during crack propagation

$$\mathcal{G}_c = \frac{\partial E_{\text{diss}}}{\partial A} \tag{16}$$

where the derivative describes how much energy is dissipated for each unitary increment of cracked area. Before taking the derivative, an exponential fit is considered to suppress the amplification of measurement uncertainties. The corresponding results are shown in Figure 16. Both cases lead to consistent results with small differences on the curvature, maximum crack length, and $\mathcal{G}_c$ level for a given face. Longer cracks are seen at the back of the specimen when the results of the two faces are compared. It is worth noting that the curve reported in Figure 16 is not physically allowed to start from $\mathcal{G}_c = 0$, since there is a minimum energy to break chemical bounds. However, this works aims to analyze propagating macrocracks, and at this scale, the resolution was not sufficient to check for the very beginning of this curve.

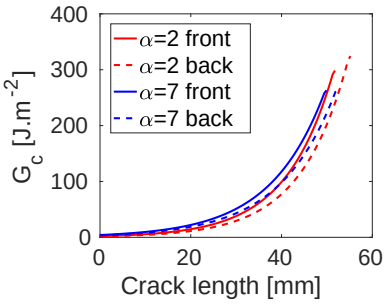

Figure 16: Global fracture energy $\mathcal{G}_c$ predicted by the studied CZMs, which are calculated from the exponential fit of the total dissipated energy. The results from the front face are in solid lines and for the back face in dashed lines.

To check these results and compare them with earlier estimates [15, 19], the mean level $\overline{\mathcal{G}}_c$ is calculated

$$\overline{\mathcal{G}}_c = \frac{1}{\Delta a_{\max}} \int_0^{\Delta a_{\max}} \mathcal{G}_c(a)\ \mathrm{d}a \tag{17}$$

where $\Delta a_{\max}$ denotes the maximum length of the damaged area. The values of $\overline{\mathcal{G}}_c$ are reported in Table 3. A good agreement is observed with the values reported in Refs. [15, 19] when integrated DIC is considered. The values are father apart with FEMU-U [19] (*i.e.,* with a cost function using displacement measurements) is used instead. With the present case, it is not possible to clearly distinguish which α is better since both yielded very low residuals and consistent results.

Table 3 compares the fracture energy predicted the proposed approach with two other independent methods applied to the same experiment. Although the methodologies reported in Refs. [15, 19] do not use CZMs, the energetic approach allows such comparisons. The fracture energies obtained with the PPR model are very close for the front and back faces, while those reported before had more significant differences. It is believed that it may related to the BC_c parameter, which corrects for the unknown fully unloaded state and was not accounted for with the other methods [15, 19]. For the finer mesh and $\alpha = 2$, the average fracture energy is found equal to 62.2 J/m^2, which is very close to the level

found with the coarser mesh (Table 3). This observation further confirms the quasi mesh independence of the results reported herein.

Table 3: Average fracture energy $\overline{\mathcal{G}}_c$ expressed in J/m^2 for the two CZMs applied to the back and front faces separately. These predictions are compared with earlier results obtained by two independent approaches (*i.e.,* integrated DIC [15] and FEMU-U [19])

model	front face	back face
PPR ($\alpha = 2$)	61.3	62.4
PPR ($\alpha = 7$)	63.5	62.2
IDIC$^\sharp$	84	52
FEMU-U$^\sharp$	162	97

$^\sharp$ according to Refs. [15, 19]

In order to improve the proposed methodology, the identification could be coupled for both faces, or even based on 3D simulations. Implementation of cohesive elements with similar approaches for cases where the crack bifurcates on the surfaces is also an interesting outlook. Last, 4D analyses via in-situ tests in x-ray tomographs may elucidate further the crack paths and fracture mechanisms taking place in such materials.

3.3.2. FPZ size

Since nonzero tractions are still predicted even close to the precrack at the end of the test, a final discussion about the FPZ size and its relationship with the material is discussed. With the identified parameters, the so-called Hillerborg size ℓ_H [20] is evaluated

$$\ell_H = \frac{EJ_c}{\sigma_{\max}^2} \tag{18}$$

and reported in Table 4. The length of the process zone is generally a fraction of ℓ_H [55]. In the present case, the FPZ length is of the order of ca. 50 mm (see Figures 12 to 16, for instance), which is one order of magnitude smaller than ℓ_H.

Table 4: ℓ_H for the studied cases in millimeters.

model	front face	back face
PPR ($\alpha = 2$)	434	604
PPR ($\alpha = 7$)	500	773

The estimate of the FPZ length leads to the conclusion that the FPZ was not yet fully developed, which is proven by the remaining stresses close to the pre-crack. This also explains the increasing energy release rate curve [56]. To further analyze the FPZ, the test should be continued until the end of the propagation, or in the case of materials with high ℓ_H as the one studied herein, a longer sample would be preferable.

The obtained fracture parameters and the FPZ length are consistent with the material microstructure and its processing. The analyzed composition is suitable for fluidized catalytic cracking units that operate in temperature ranges of 550 to 800 °C. Such materials are not sintered in situ as other refractories, and thus, their resistance strongly depends on the hydraulic bindings and packing of the raw material [57]. As this specimen was fired at low temperature (*i.e.,* 500 °C [19]), it is expected to have aggregates weakly bonded to the matrix and microcracks related to the anisotropy of the phases [57]. The initiation of a crack is easy in such materials, which explains the low level of the cohesive strength σ_{max}. Since the specimen cannot store much elastic energy prior to crack initiation (*i.e.,* the elastic energy is proportional to σ_{max}^2), the latter is easy and occurs very early on, and subsequent crack branches and bridging are possible, thereby dissipating more energy through friction and leading to a considerably higher J_c. In the present case, it is believed that crack bridging is the most likely mechanism since no branches were detected macroscopically on the investigated faces [19]. All these effects result in a large FPZ that in the case investigated herein spans over all the propagation path.

4. Conclusions

A FEMU-F methodology was applied to calibrate cohesive properties, *i.e.,* the cohesive strength (σ_{max}) and the fracture energy (J_c), of the so-called PPR model. Only the reaction forces were considered in the cost function to be minimized. By using the geometry seen on digital images to build the FE mesh, T3DIC results were directly used as boundary conditions to drive the simulations. The same region being used in T3DIC and FE analyses also allowed the experimental displacements to be compared with the simulated kinematics. The Hessian matrix was directly analyzed to infer the conditioning and sensitivity of the identification scheme to the sought parameters. It was also proposed to add a third parameter related to the correction of the applied boundary conditions.

The two studied softening regimes of the cohesive law resulted in similar material properties. Both σ_{max} and J_c were identified in the range of castable refractories, with values close to identifications obtained via integrated DIC [15, 19]. The cohesive strengths were very close on both analyzed faces of the sample, while some deviation of the order of 20 % was reported for the fracture energy. However, the dissipated energy was similar for both sides of the sample. The parameters identified for the cohesive law allowed the Hillerborg length to be calculated. When coupled with the traction space-time history of the cohesive elements, it gives insight into FPZ length. The boundary condition corrections were significantly different for both analyzed faces, thereby emphasizing that the wedge was slightly tilted at pre-load. It is worth noting that the thickness of the specimen combined with the presence of aggregates on the composition makes it difficult to perfectly align the wedge. However, the proposed approach showed robustness to tackle this misalignment.

The present study shows the feasibility of modeling crack propagation of castable refractories tested in the WST with cohesive elements. Cohesive parameters were calibrated with good correlations to previously reported fracture parameters for the same experiment. The residuals in force, displacement and gray level were very close to the noise level, which validates the methodology

and the investigated model. Given the fact that damage did not reach its maximum value explains why an ever increasing R-curve response was observed. This means that the extent of the process zone spans over most of the crack surface. The rather long fracture process zone is related to a low tensile strength (*i.e.*, easy crack initiation) and high fracture energy. It is believed that most of the energy is dissipated through friction by aggregate bridging in the present case, since they are weakly bonded to the matrix after low temperature firing.

Acknowledgments

JAR thanks CNPq for the productivity scholarship, grant #307127/2013-3. RV's stay at LMT was supported through an RIA scholarship, grant #2017/20911-9, São Paulo Research Foundation (FAPESP).

References

[1] Lee WE, Vieira W, Zhang S, Ghanbari Ahari K, Sarpoolaky H, Parr C. Castable refractory concretes. International Materials Reviews 2001;46(3):145–67.

[2] Wachtman J. Materials and Equipment - Whitewares - Refractory Ceramics - Basic Science: Ceramic Engineering and Science Proceedings, Volume 16. No. 1 in Ceramic Engineering and Science Proceedings; Wiley; 2009. ISBN 9780470316306.

[3] Luz AP, Braulio MAL, Pandolfelli VC. Refractory Castable Engineering; vol. 1. 1 ed.; São Carlos, SP: Göller Verlag; 2015.

[4] Lee WE, Moore RE. Evolution of in situ refractories in the 20th century. Journal of the American Ceramic Society 1998;81(6):1385–410.

[5] Steinbrech RW. R-curve behavior of ceramics. In: Bradt R, Hasselman D, Munz D, Sakai M, Shevchenko V, editors. Fracture Mechanics of Ceramics; vol. 9 of Fracture Mechanics of Ceramics. Springer US. ISBN 978-1-4613-6477-1; 1992, p. 187–208.

[6] Launey ME, Ritchie RO. On the fracture toughness of advanced materials. Advanced Materials 2009;21(20):2103–10.

[7] Tschegg E. Prüfeinrichtung zur Ermittlung von bruchmechanishen Kennwerten sowie hiefür geeignete, Prüfkörper, Austrian Pat. AT 390328B, registered. 1986.

[8] Brühwiler E, Wittmann FH. The wedge splitting test, a new method of performing stable fracture mechanics tests. Engineering Fracture Mechanics 1990;35(1-3):117–25.

[9] Ribeiro S, Rodrigues JA. The influence of microstructure on the maximum load and fracture energy of refractory castables. Ceramics International 2010;36(1):263–74.

[10] Miyaji DY, Tonnesen T, Rodrigues JA. Fracture energy and thermal shock damage resistance of refractory castables containing eutectic aggregates. Ceramics International 2014;40(9, Part B):15227–39.

[11] Sutton MA, McNeill SR, Helm JD, Chao YJ. Advances in two-dimensional and three-dimensional computer vision. In: Photomechanics; vol. 77 of Topics in Applied Physics. 2000, p. 323–72.

[12] Sutton MA, Orteu JJ, Schreier H. Image correlation for shape, motion and deformation measurements: basic concepts, theory and applications. Springer Science & Business Media; 2009.

[13] Sutton MA. Computer vision-based, noncontacting deformation measurements in mechanics: A generational transformation. Applied Mechanics Reviews 2013;65(AMR-13-1009, 050802).

[14] Belrhiti Y, Pop O, Germaneau A, Doumalin P, Dupré JC, Harmuth H, et al. Investigation of the impact of micro-cracks on fracture behavior of magnesia products using wedge splitting test and digital image correlation. Journal of the European Ceramic Society 2015;35(2):823–9.

[15] Vargas R, Neggers J, Canto RB, Rodrigues JA, Hild F. Analysis of wedge splitting test on refractory castable via integrated DIC. Journal of the European Ceramic Society 2016;36(16):4309–17.

[16] Dai Y, Gruber D, Harmuth H. Observation and quantification of the fracture process zone for two magnesia refractories with different brittleness. Journal of the European Ceramic Society 2017;37(6):2521–9.

[17] Dai Y, Gruber D, Harmuth H. Determination of the fracture behaviour of MgO-refractories using multi-cycle wedge splitting test and digital image correlation. Journal of the European Ceramic Society 2017;37(15):5035–43.

[18] Dupré JC, Doumalin P, Belrhiti Y, Khlifi I, Pop O, Huger M. Detection of cracks in refractory materials by an enhanced digital image correlation technique. Journal of Materials Science 2018;53(2):977–93.

[19] Vargas R, Neggers J, Canto RB, Rodrigues JA, Hild F. Comparison of two full-field identification methods for the wedge splitting test on a refractory. Journal of the European Ceramic Society 2018;38(16):5569 –79.

[20] Hillerborg A, Modéer M, Petersson PE. Analysis of crack formation and crack growth in concrete by means of fracture mechanics and finite elements. Cement and Concrete Research 1976;6(6):773–82.

[21] Elices M, Guinea G, Gómez J, Planas J. The cohesive zone model: advantages, limitations and challenges. Engineering Fracture Mechanics 2002;69:137–63.

[22] Dugdale DS. Yielding of steel sheets containing slits. Journal of the Mechanics and Physics of Solids 1960;8(2):100 –4.

[23] Song SH, Paulino GH, Buttlar WG. Simulation of crack propagation in asphalt concrete using an intrinsic cohesive zone model. Journal of Engineering Mechanics 2006;132(11):1215–23.

[24] Aure T, Ioannides A. Simulation of crack propagation in concrete beams with cohesive elements in abaqus. Transportation Research Record: Journal of the Transportation Research Board 2010;(2154):12–21.

[25] Su X, Yang Z, Liu G. Finite Element Modelling of Complex 3D Static and Dynamic Crack Propagation by Embedding Cohesive Elements in Abaqus. Acta Mechanica Solida Sinica 2010;23(3):271 –82.

[26] Evangelista F, Roesler JR, Proença SP. Three-dimensional cohesive zone model for fracture of cementitious materials based on the thermodynamics of irreversible processes. Engineering Fracture Mechanics 2013;97:261–80.

[27] Shen B, Paulino GH. Identification of cohesive zone model and elastic parameters of fiber-reinforced cementitious composites using digital image correlation and a hybrid inverse technique. Cement and Concrete Composites 2011;33(5):572–85.

[28] Shen B, Paulino GH. Direct extraction of cohesive fracture properties from digital image correlation: a hybrid inverse technique. Experimental Mechanics 2011;51(2):143–63.

[29] Fedele R, Sessa S, Valoroso N. Image correlation-based identification of fracture parameters for structural adhesives. Technische Mechanik 2012;32(2):195–204.

[30] Alfano M, Lubineau G, Paulino GH. Global sensitivity analysis in the identification of cohesive models using full-field kinematic data. International Journal of Solids and Structures 2015;55:66–78.

[31] Blaysat B, Hoefnagels JPM, Lubineau G, Alfano M, Geers MGD. Interface debonding characterization by image correlation integrated with double cantilever beam kinematics. International Journal of Solids and Structures 2015;55:79–91.

[32] Affagard JS, Mathieu F, Guimard JM, Hild F. Identification method for the mixed mode interlaminar behavior of a thermoset composite using displacement field measurements and load data. Composites Part A: Applied Science and Manufacturing 2016;91:238–49.

[33] Ruybalid AP, Hoefnagels JPM, van der Sluis O, van Maris MPFHL, Geers MGD. Mixed-mode cohesive zone parameters from integrated digital image correlation on micrographs only. International Journal of Solids and Structures 2018;.

[34] Abanto-Bueno J, Lambros J. Experimental determination of cohesive failure properties of a photodegradable copolymer. Experimental Mechanics 2005;45(2):144–52.

[35] Ferreira M, Venturini W, Hild F. On the analysis of notched concrete beams: From measurement with digital image correlation to identification with boundary element method of a cohesive model. Engineering Fracture Mechanics 2011;78(1):71 – 84.

[36] Richefeu V, Chrysochoos A, Huon V, Monerie Y, Peyroux R, Wattrisse B. Toward local identification of cohesive zone models using digital image correlation. European Journal of Mechanics-A/Solids 2012;34:38–51.

[37] Rethore J, Estevez R. Identification of a cohesive zone model from digital images at the micron-scale. Journal of the Mechanics and Physics of Solids 2013;61(6):1407–20.

[38] Abaqus 6.14 Documentation. Dassault Systèmes Simulia Corp.; Providence, RI, USA.; 2014.

[39] Diógenes HJF, Cossolino LC, Pereira AHA, El Debs MK, El Debs ALHC. Determination of modulus of elasticity of concrete from the acoustic response. Revista IBRACON de Estruturas e Materiais 2011;4(5):803–13.

[40] Hild F, Bouterf A, Chamoin L, Leclerc H, Mathieu F, Neggers J, et al. Toward 4D mechanical correlation. Advanced Modeling and Simulation in Engineering Sciences 2016;3(1):17.

[41] Besnard G, Hild F, Roux S. "Finite-Element" displacement fields analysis from digital images: Application to Portevin-Le Chatelier bands. Experimental Mechanics 2006;46(6):789–803.

[42] Leclerc H, Périé J, Roux S, Hild F. Integrated digital image correlation for the identification of mechanical properties; vol. LNCS 5496. Berlin (Germany): Springer; 2009, p. 161–71.

[43] Geuzaine C, Remacle JF. Gmsh: A 3-D finite element mesh generator with built-in pre-and post-processing facilities. International Journal for Numerical Methods in Engineering 2009;79(11):1309–31.

[44] Hild F, Roux S. Comparison of local and global approaches to digital image correlation. Experimental Mechanics 2012;52(9):1503–19.

[45] Pagnacco E, Caro-Bretelle AS, Ienny P. Parameter Identification from Mechanical Field Measurements using Finite Element Model Updating Strategies; chap. 9. Wiley-Blackwell; 2012, p. 247–74.

[46] Maginador RV. Analysis of crack propagation in the Wedge Splitting Test via Digital Image Correlation and Finite Element Analyses. Master's thesis; Federal University of São Carlos (UFSCar) - Brazil; 2019.

[47] Park K, Paulino GH, Roesler JR. A unified potential-based cohesive model of mixed-mode fracture. Journal of the Mechanics and Physics of Solids 2009;57(6):891–908.

[48] Park K, Paulino GH. Computational implementation of the PPR potential-based cohesive model in ABAQUS: educational perspective. Engineering Fracture Mechanics 2012;93:239–62.

[49] Park K, Choi H, Paulino GH. Assessment of cohesive traction-separation relationships in ABAQUS: A comparative study. Mechanics Research Communications 2016;78:71–8.

[50] Fedele R, Raka B, Hild F, Roux S. Identification of adhesive properties in GLARE assemblies using digital image correlation. Journal of the Mechanics and Physics of Solids 2009;57(7):1003–16.

[51] Falk ML, Needleman A, Rice JR. A critical evaluation of cohesive zone models of dynamic fracture. In: Proceedings of the 5th European mechanics of materials conference on scale transitions from atomistics to continuum plasticity. 2001, p. 43–50.

[52] Davila C, Camanho P, de Moura M. Mixed-mode decohesion elements for analyses of progressive delamination. In: 19th AIAA Applied Aerodynamics Conference. 2001, p. 1486.

[53] Moës N, Belytschko T. Extended finite element method for cohesive crack growth. Engineering Fracture Mechanics 2002;69(7):813–33.

[54] Moslemi M, Khoshravan M. Cohesive zone parameters selection for mode-I prediction of interfacial delamination. Strojniski Vestnik/Journal of Mechanical Engineering 2015;61(9):507–16.

[55] Saucedo L, Rena CY, Ruiz G. Fully-developed FPZ length in quasi-brittle materials. International Journal of Fracture 2012;178(1-2):97–112.

[56] Dong W, Zhou X, Wu Z. On fracture process zone and crack extension resistance of concrete based on initial fracture toughness. Construction and Building Materials 2013;49:352–63.

[57] Pereira AHA, Miyaji DY, Cabrelon MD, Medeiros J, Rodrigues JA. A study about the contibution of the α-β phase transition of quartz to thermal cycle damage of a refractory used in fluidized catalytic cracking units. Cerâmica 2014;60:449–56.

Appendix A

The space-time history of the cohesive tractions for the back face is shown for the two analyzed cases in Figure 17. When $\alpha = 7$, the damaged zone is smaller and develops later on. At the end of the test, the extent of the damaged zones is similar in both cases.

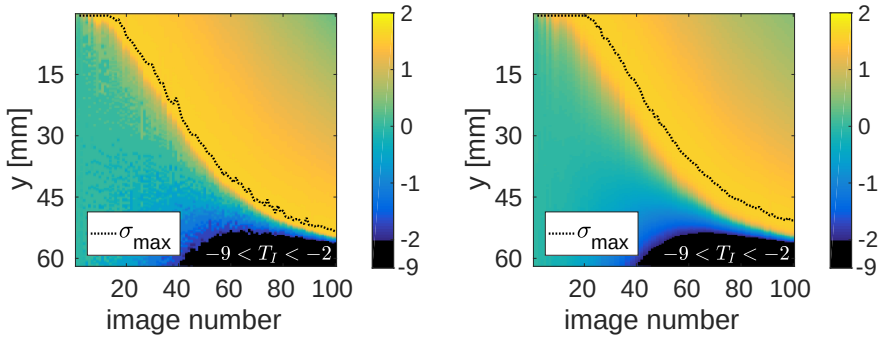

Figure 17: Normal traction (expressed in MPa) history for the back face, with $\alpha = 2$ (a) and $\alpha = 7$ (b). The black dotted line shows the location for which the cohesive strength $\sigma_{\max}$ was reached.

The damage history for the back face is shown in Figure 18. Although the most damaged element reaches a level less than 0.9, most of the specimen is damaged at the end of the test. This observation applies in both cases.

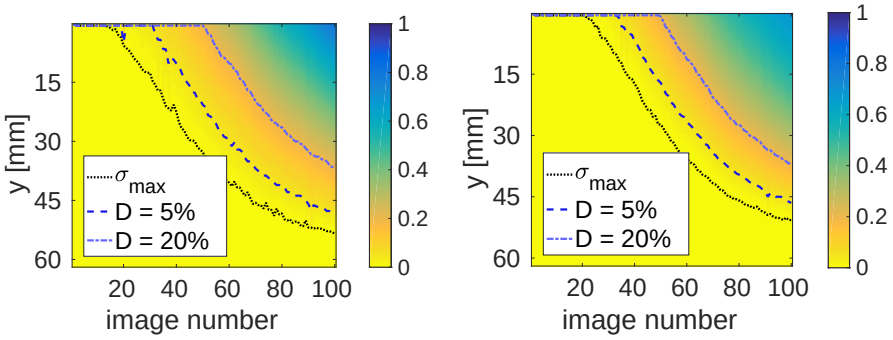

(a) (b)

Figure 18: Damage history for the back face with $\alpha = 2$ (a) and $\alpha = 7$ (b). The black dotted line shows the location for which the cohesive strength $\sigma_{\max}$ was reached.

The spacetime history of elementary dissipated energy for the back face is shown in Figure 19. The maximum level that can be reached is equal to J_c, but no element has achieved such dissipation in both cases.

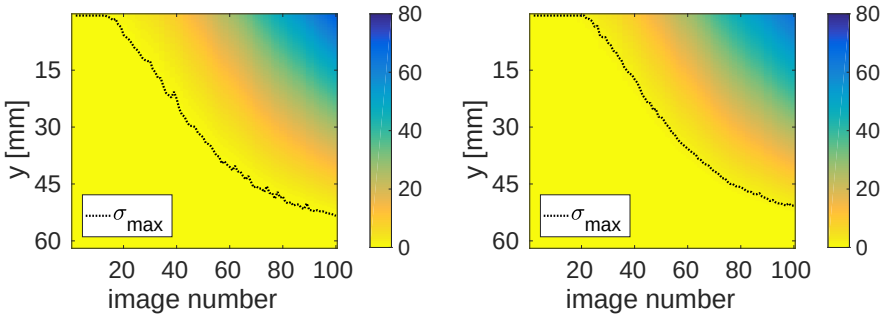

(a) (b)

Figure 19: Elementary dissipated energy (in J/m^2) history for the back face when $\alpha = 2$ (a) and $\alpha = 7$ (b). The black dotted line shows the location for which the cohesive strength $\sigma_{\max}$ was reached.